



Article

# Synergistic Effects on Incorporation of $\beta$ -Tricalcium Phosphate and Graphene Oxide Nanoparticles to Silk Fibroin/Soy Protein Isolate Scaffolds for Bone Tissue Engineering

Fan Liu <sup>1,2</sup> , Chen Liu <sup>1</sup>, Bowen Zheng <sup>2</sup>, Jia He <sup>2</sup>, Jun Liu <sup>2</sup>, Cen Chen <sup>3</sup>, In-seop Lee <sup>4</sup>, Xiaohong Wang <sup>1,5,\*</sup> and Yi Liu <sup>2,\*</sup> 

<sup>1</sup> Center of 3D Printing & Organ Manufacturing, School of Fundamental Sciences, China Medical University (CMU), No. 77 Puhe Road, Shenyang North New Area, Shenyang 110122, China; liufan-sky@163.com (F.L.); 18856152351@163.com (C.L.)

<sup>2</sup> Department of Orthodontics, School of Stomatology, China Medical University, Shenyang 110122, China; zhengbowen1991@126.com (B.Z.); hejia\_777@163.com (J.H.); liu18240293491@163.com (J.L.)

<sup>3</sup> College of Life Sciences, Zhejiang Sci-Tech University, Hangzhou 310018, China; ci0\_0ci@hotmail.com

<sup>4</sup> Institute of Natural Sciences, Yonsei University, Seoul 120-749, Korea; inseop@yonsei.ac.kr

<sup>5</sup> Center of Organ Manufacturing, Department of Mechanical Engineering, Tsinghua University, Beijing 100084, China

\* Correspondence: wangxiaohong709@163.com or wangxiaohong@tsinghua.edu.cn (X.W.); Liuyi@cmu.edu.cn (Y.L.); Tel.: +86-24-31900983 (X.W.); +86-24-31973999 (Y.L.)

Received: 3 December 2019; Accepted: 16 December 2019; Published: 2 January 2020



**Abstract:** In bone tissue engineering, an ideal scaffold is required to have favorable physical, chemical (or physicochemical), and biological (or biochemical) properties to promote osteogenesis. Although silk fibroin (SF) and/or soy protein isolate (SPI) scaffolds have been widely used as an alternative to autologous and heterologous bone grafts, the poor mechanical property and insufficient osteoinductive capability has become an obstacle for their in vivo applications. Herein,  $\beta$ -tricalcium phosphate ( $\beta$ -TCP) and graphene oxide (GO) nanoparticles are incorporated into SF/SPI scaffolds simultaneously or individually. Physical and chemical properties of these composite scaffolds are evaluated using field emission scanning electron microscope (FESEM), X-ray diffraction (XRD) and attenuated total reflectance Fourier transformed infrared spectroscopy (ATR-FTIR). Biocompatibility and osteogenesis of the composite scaffolds are evaluated using bone marrow mesenchymal stem cells (BMSCs). All the composite scaffolds have a complex porous structure with proper pore sizes and porosities. Physicochemical properties of the scaffolds can be significantly increased through the incorporation of  $\beta$ -TCP and GO nanoparticles. Alkaline phosphatase activity (ALP) and osteogenesis-related gene expression of the BMSCs are significantly enhanced in the presence of  $\beta$ -TCP and GO nanoparticles. Especially,  $\beta$ -TCP and GO nanoparticles have a synergistic effect on promoting osteogenesis. These results suggest that the  $\beta$ -TCP and GO enhanced SF/SPI scaffolds are promising candidates for bone tissue regeneration.

**Keywords:** graphene oxide;  $\beta$ -tricalcium phosphate; silk fibroin; soy protein isolate; scaffold; osteogenesis

## 1. Introduction

Bone deformities from congenital deformity, traumatic injury, and oncologic resection severely affect patients' physical function and mental health. Although autologous, allograft, or xenograft bone transplantations can repair dysfunctional or defect bones in clinic, many limitations still need to be addressed: transplanted bone infection or instability, insufficient transplanted volume,

even immunological rejection [1–3]. Thus, bone tissue engineering, involving the fabrication of three-dimensional porous scaffolds and seeding osteogenesis cells with biologically active factors on the porous scaffolds, has merged as a solution to replace traditional bone repair methods [4]. Among them, hybrid biodegradable scaffolds are of increasing interest as a strategy in recent years.

Silk fibroin (SF), a protein derived from *Bombyx mori* silkworm cocoons, is a promising natural polymer that has excellent biocompatibility and controllable degradability [5,6]. Although SF scaffolds have been reported to support mesenchymal stem cell (MSC) attachment, proliferation, and extracellular matrix (ECM) deposition [7], it is insufficient to induce stem cell differentiation, and even repair large bone defects. Thus, blending of SF with other polymers is expected to develop double-network composite scaffolds that enhance biological properties [8]. Among them, soy protein isolate (SPI), a dietary protein extracted from the soy bean, has emerged as an attractive alternative to animal-derived protein source for biomedical applications. It contains various bioactive peptides, and has been approved by the Food and Drug Administration (FDA) of the United States for its potential health benefits. SPI could significantly improve trabecular number, bone volume, and bone mineral density in mice [9,10]. More importantly, some researches indicated that SPI might counteract the detrimental effects of osteoporosis and obesity by regulating a series of signal pathways, correcting the imbalance of remodeling [11].

Graphene oxide (GO), prepared by oxidation of graphite, is a two-dimensional carbon-based nanomaterial with many hydrophilic functional groups (i.e., hydroxyl, carboxyl and epoxy groups), favorable biocompatibility and physiochemical stability compared with pristine graphene [12]. However, bulk graphene-based porous structures have small pore sizes and lack enough mechanical strengths, leading to low cell adhesion and slow migration on these surfaces [13,14]. Also, cytotoxicity is related to the size, shape and concentration of GO nanoparticles, which need to be carefully considered [15,16]. It is noteworthy that GO can be readily functionalized with other materials because of its large specific surface area, as well as hydrophilic groups,  $\pi$ - $\pi$  stacking framework and electrostatic interactions [17,18].

In recent years, the use of calcium phosphate ceramics (CaPs) is of increasing interest as a strategy to design the inorganic part of biomimetic scaffolds. Among the CaPs,  $\beta$ -tricalcium phosphate ( $\beta$ -TCP) has good biocompatibility, osteoconductivity, and resorbability, which can form a fast fixation and chemical connection with bone [19–22].

Herein, we hypothesize that incorporating  $\beta$ -TCP and GO nanoparticles into the SF/SPI scaffolds could invariably improve the physicochemical and biological properties, particularly, enhance osteoinductive capability of the SF/SPI scaffolds. The objective of our study is to investigate the synergistic effect on promoting the osteogenic differentiation of bone marrow mesenchymal stem cells (BMSCs) in the presence of  $\beta$ -TCP and GO nanoparticles. A series of SF/SPI-based composite scaffolds for bone tissue engineering are fabricated by incorporating  $\beta$ -TCP and GO nanoparticles simultaneously or individually. The physical, chemical and biological properties of these SF/SPI-based composite scaffolds are evaluated.

## 2. Materials and Methods

### 2.1. Preparation of Silk Fibroin Solution

Aqueous SF solution was prepared based on a previously reported procedure [23]. Briefly, 8 g *Bombyx mori* cocoon was finely cut into pieces, and boiled in an aqueous solution of 0.02 M  $\text{Na}_2\text{CO}_3$  for 60 min. After being rinsed with deionized water three times, the samples were dehydrated into an oven at 60 °C overnight. The dried silk fibroin was sequentially dissolved in 100 mL 9.3 M LiBr solution, and kept stirring until complete dissolution at 60 °C. Then, the solution was dialyzed in deionized water, using a dialysis tube with molecular weight cutoff of 10,000 Da for three days. The dialyzed SF solution was centrifuged at 6000 r/min for 10 min to remove the insoluble part, and was stored at 4 °C.

## 2.2. Fabrication of SF/SPI-Based Composite Scaffolds

SF/SPI-based composite scaffolds containing SF, SPI,  $\beta$ -TCP, and GO were prepared by a freeze-drying method. First, SF and SPI were prepared as 4% (*w/v*) stock solutions in distilled water respectively. The SF and SPI solutions were mixed in the volume ratio of 1:1, and was kept stirring at room temperature until there were no bubbles. Then,  $\beta$ -TCP and GO particles were sequentially added into the mixed SF/SPI solution in the ratio of 10 mg:10 mg:10 mL, and transferred to a 48-well plate and frozen at  $-80\text{ }^{\circ}\text{C}$  for 24 h followed by lyophilization. The lyophilized scaffolds were immersed in the 4-morpholine ethane sulfonic acid (MES) buffer solution (50 mmol/L, 70% ethanol solution) containing EDC/NHS (EDC 50 mmol/L, NHS 25 mol/L) for 24 h at room temperature as crosslinking step [24,25]. The crosslinked scaffolds were immersed into 75% ethanol and deionized water to rinse the redundant crosslinking reagent, and frozen at  $-80\text{ }^{\circ}\text{C}$  for 24 h, followed by vacuum drying for 36 h (SCIENTZ-10N, SCIENTZ, Ningbo, China). At last, the SF/SPI/GO/ $\beta$ -TCP composite scaffolds were stored in a container for future use. To fabricate SF/SPI, SF/SPI/ $\beta$ -TCP and SF/SPI/GO scaffolds, the above protocol was followed in where the addition of  $\beta$ -TCP or GO was excluded.

## 2.3. Characterization of the SF/SPI-Based Composite Scaffolds

### 2.3.1. Morphologies of the SF/SPI-Based Composite Scaffolds

Surface morphologies of the prepared samples were observed by a field emission scanning electron microscope (FESEM) (XL-30, Philips, NLD, Amsterdam, The Netherlands). The samples were first sputter-coated with gold using ion sputter. FESEM photographs were obtained at magnifications of 500 $\times$  and 5000 $\times$  with an acceleration voltage of 15 kV.

### 2.3.2. Compositions of the SF/SPI-Based Composite Scaffolds

Chemical composition of the prepared samples were analyzed via a X-ray diffraction (XRD) (X' Pert<sup>3</sup> Powder, PANalytical, NLD, Amsterdam, The Netherlands) and attenuated total reflectance Fourier transformed infrared spectroscopy (ATR-FTIR) (VERTEX 70, Bruker, GER, Billerica, MA, USA). XRD analysis was performed using a Cu-K $\alpha$  source, and the spectrum were recorded from 8 to 80 $^{\circ}$  2 theta at 36 kV. All characteristic peaks were identified in the International Centre for Diffraction Data (ICDD) database. ATR-FTIR was used to analyze the chemical compositions of different samples. The spectra were recorded from 4000–400  $\text{cm}^{-1}$  with a 2  $\text{cm}^{-1}$  resolution and 20 scans.

### 2.3.3. Pore Size and Porosity of the SF/SPI-Based Composite Scaffolds

Porosity of all scaffolds was measured using a previously described liquid displacement method [26]. All samples were first cut into the same size, and completely immersed into measuring cylinder with a known volume of anhydrous ethanol (V1). The volume after the immersion of all sample scaffolds was recorded (V2). Finally, the ethanol-impregnated scaffolds were removed from the measuring cylinder. The residual ethanol volume was recorded (V3). The porosity (P) of the scaffold was calculated through the following equation. Each test was performed in three independent preparations.

$$P = [(V1 - V3)/(V2 - V3)] \times 100\% \quad (1)$$

### 2.3.4. Water Adsorption of the SF/SPI-Based Composite Scaffolds

Water adsorption behaviors (swelling ratios) of the SF/SPI-based composite scaffolds were measured using a gravimetric method. All sample scaffolds were cut into the same size. The weight of dry sample scaffolds was recorded (M0). After immersion into PBS solution for 24 h, the excess water was removed using a filter paper. The sample scaffolds were then dried in an oven at 60  $^{\circ}\text{C}$  under vacuum overnight, and the dry weight of the scaffolds (M1) was recorded.

$$\text{Water adsorption ratio (\%)} = [(M0 - M1)/M0] \times 100\% \quad (2)$$

### 2.3.5. In Vitro Mineralization of the SF/SPI-Based Composite Scaffolds

In vitro mineralization was performed by immersing the SF/SPI-based composite scaffolds into simulated body fluid (SBF). The SBF solution was prepared as reported in a previous work [27]. All the prepared samples ( $1 \times 1 \times 1 \text{ cm}^3$ ) were immersed in the 5 mL SBF solution and incubated at  $37^\circ\text{C}$  for 1, 3, 7, and 14 days. At the planned time point, the samples were rinsed with deionized water and subsequently lyophilized. The formed apatite on surface of all SF/SPI-based scaffolds was observed using scanning electron microscope (SEM) (XL-30, Philips, NLD, Amsterdam, The Netherlands) after being immersed into the SBF solution at different time points, while the formed apatite composition was determined using XRD with the scanning angles between  $20^\circ$  and  $70^\circ$  on 14th day.

### 2.3.6. Mechanical Properties of the SF/SPI-Based Composite Scaffolds

Mechanical properties of the SF/SPI-based composite scaffolds were calculated using a Universal Testing Machine (Instron 5967, Instron LTD, Boston, MA, USA). A 0.5 force was loaded on sample scaffolds with a measuring speed of 20 mm/min. Three tests for compressive strength were performed in each sample.

## 2.4. In Vitro Biocompatibility and Osteogenic Evaluation of the SF/SPI-Based Composite Scaffolds

### 2.4.1. Morphology and Viability of BMSCs on the SF/SPI-Based Composite Scaffolds

Sprague-Dawley (SD) rat bone marrow mesenchymal stem cells (BMSCs) (Cyagen Biociences, Guangzhou, China) were cultured in BMSCs growth medium (Cyagen Biociences, Guangzhou, China) containing 10% fetal bovine serum (FBS) and 1% antibiotic-antimycotic at  $37^\circ\text{C}$  with 5%  $\text{CO}_2$ . The culture medium was changed every two days until the cells reached 80–90% confluence. The third cell passage was used for proliferative evaluation, and the fifth cell passage was used for differentiation.

Cells were cultured at a density of  $2 \times 10^4$  per sample on the SF/SPI-based composite scaffolds for 1, 3, 5, and 7 days. Cell morphology on each scaffold was observed at 48 h using SEM and confocal microscopy. Cell viability was evaluated using Cell Counting Kit-8 (CCK-8, Beyotime, Shanghai, China). The scaffolds of SF/SPI/GO and SF/SPI/GO/ $\beta$ -TCP without cell seeding are used as controls. At each time point, the samples were washed twice with PBS. Fresh culture medium (200  $\mu\text{L}$ ) was mixed with 20  $\mu\text{L}$  of CCK-8 reagent and added to each sample. Then, the culture was incubated at  $37^\circ\text{C}$  for 2 h. After the incubation, 100  $\mu\text{L}$  of the medium was transferred to a 96-well plate and measured at 450 nm.

### 2.4.2. Cell Cytoskeletal Organization of BMSCs on the SF/SPI-Based Composite Scaffolds

BMSCs were seeded on the SF/SPI-based composite scaffolds at a density of  $4 \times 10^5$  cells per sample. For actin staining, cells were washed gently with PBS, and fixed with 10% neutral buffered formalin for 15 min at room temperature. The cells were permeabilized using 0.5% Triton X-100 in PBS for 5 min. After being washed with PBS for 10 min twice, the cells were incubated with rhodamine-conjugated phalloidin (CA1610, Solarbio, Beijing, China) for 30 min in the dark followed by counterstaining with 4',6-diamidino-2-phenylindole (DAPI) to visualize the nuclei. Images were captured at  $40\times$  magnification with a confocal microscope (Nikon AIR, Nikon, Tokyo, Japan).

### 2.4.3. Alkaline Phosphatase Activity of BMSCs on the SF/SPI-Based Composite Scaffolds

ALP activity is regarded as a marker of early stage osteogenic expression. Cells were seeded at a density of  $2 \times 10^4$  per sample on the SF/SPI-based composite scaffold for 3, 5, or 14 days. ALP activity of the BMSCs was measured using ALP assay kit (Beyotime, Shanghai, China) which was based on the color reaction of colorless *p*-nitrophenyl phosphate (pNPP) converted to yellow *p*-nitrophenol after incubation at  $37^\circ\text{C}$  for 30 min. Briefly, the original culture medium was removed, and the cells were washed twice with PBS at each time point, and sequentially lysed using RIPA lysis buffer. After

centrifugation at 5000 rpm for 10 min, the supernatant was transferred into 96-well plate. The substrates and *p*-nitrophenol were added in sequence and incubated at 37 °C for 30 min. Finally, the reaction was stopped by the addition of 100 µL stop buffer and the absorbance at 405 nm was measured.

#### 2.4.4. Osteogenesis-Related Gene Expression of BMSCs on the SF/SPI-Based Composite Scaffolds

Runt-related transcription factor 2 (Runx 2), osteocalcin (OC), and collagen type I (Col I) are representative osteogenesis-related gene markers. Quantitative real-time reverse transcription polymerase chain reaction (qRT-PCR) was performed to evaluate the osteogenesis-related gene expression of BMSCs cultured on the SF/SPI-based scaffolds on day 7 and 14. At each time point, the total RNA from each sample was first extracted using TRIzol solution (Life Technologies, Carlsbad, CA, USA), and the concentration was determined with the spectrophotometer (NanoDrop 22 Technologies, Shanghai, China). The primer sequences used for PCR amplification are listed in Table 1. The gene expression levels were calculated using the  $2^{-\Delta\Delta CT}$  method.

**Table 1.** Primers for qRT-PCR.

Genes	Forward Primer	Reverse Primer
Runx2	CGCCTCACAAACAACCACAG	TCACTGTGCTGAAGAGGCTG
OC	CATGAAGGCTTTGTCAGACT	CTCTCTCTGCTCACTCTGCT
Col I	CCACCCCAGGGATAAAAACCT	GGAGAGGAGTGCCAACTCCAG
GAPDH	AGTGCCAGCCTCGTCTCATA	GATGGTGATGGGTTTCCCGT

#### 2.5. Statistics Analysis

Statistical analysis was performed using SPSS 15.0 software. All data are depicted as mean ± standard deviation values. Multi-factor analysis of variance was first used to evaluate the statistical significance among five groups. Paired t test was used to evaluate the differences between each of the two groups at four or eight weeks. A *p* value of less than 0.05 was considered as statistically significant.

### 3. Results

#### 3.1. Physical and Chemical Properties of the SF/SPI-Based Composite Scaffolds

##### 3.1.1. Morphologies of the SF/SPI-Based Composite Scaffolds

Generally, all scaffolds display cylindrical porous structures, with a diameter of 9 mm and thickness of 6 mm fabricated through the freeze-drying method (Figure 1). The microstructures of the SF/SPI-based composite scaffolds were characterized with SEM as shown in Figure 2. All scaffolds represent similar microporous morphology and good connectivity between the pores. Most of the SF and SF/SPI scaffolds exhibit ellipse-shaped pores with rounded pore edges (Figure 2A,B). Obviously, the scaffolds display a flake-like structure with sharp pore edges when β-TCP is incorporated (Figure 2D,E). The shapes of the pore edges are altered when the β-TCP or GO nanoparticles appear on the surface of the hole walls (Figure 2C–E). These changes can be detected from the magnified images on the top right corner of each figures (Figure 2A–E).

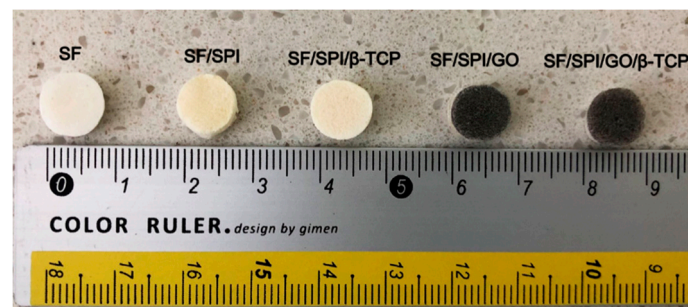


**Figure 1.** General observation of the SF/SPI-based composite scaffolds.

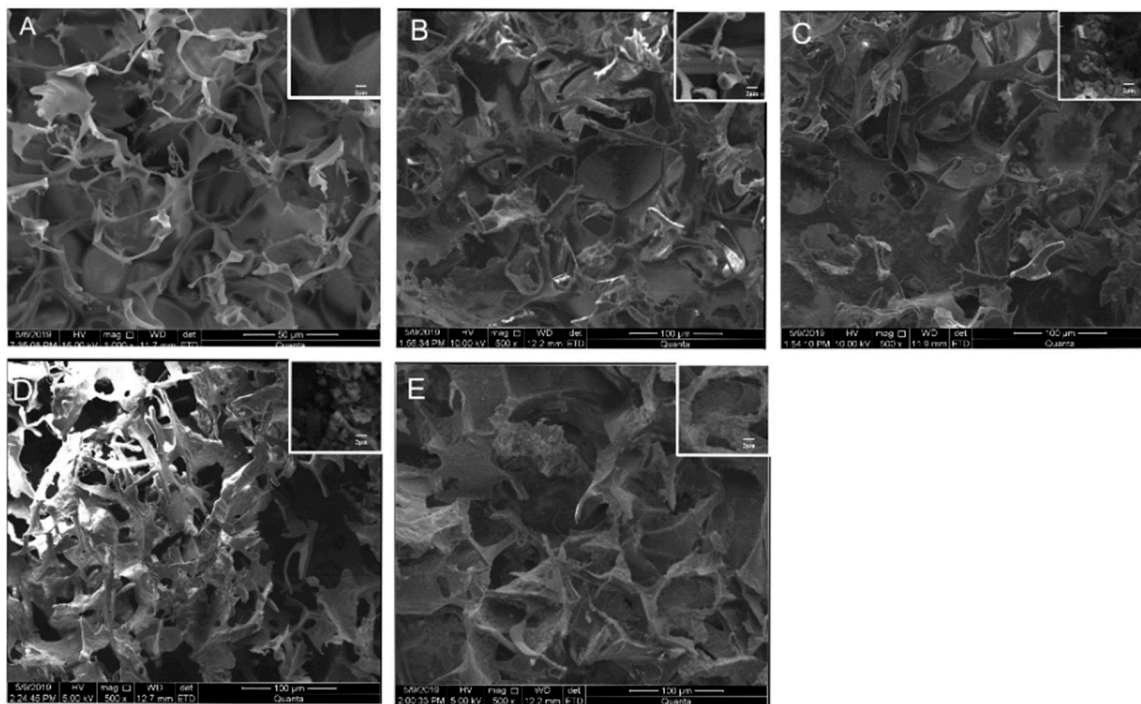


**Figure 2.** Surface morphology of the silk fibroin/soy protein isolate (SF/SPI)-based composite scaffolds ((A): SF; (B): SF/SPI; (C): SF/SPI/graphene oxide (GO); (D): SF/SPI/ $\beta$ -tricalcium phosphate ( $\beta$ -TCP); (E): SF/SPI/GO/ $\beta$ -TCP). Enlarged views of the pore structures are on the top right corner of each figures.

The pore sizes and porosities of the composite scaffolds are summarized in Table 2. The SF scaffold has the smallest pore size ( $117.76 \pm 6.33 \mu\text{m}$ ), while no significant difference is found on the scaffolds after loading of SPI. The pore sizes of the SF/SPI and SF/SPI/GO scaffolds are  $113.37 \pm 6.33$  and  $108 \pm 6.33 \mu\text{m}$ , respectively. The pore sizes of the SF/SPI/ $\beta$ -TCP and SF/SPI/ $\beta$ -TCP/GO scaffolds increase in the presence of  $\beta$ -TCP, which are significantly larger than those of the other scaffolds ( $232.53 \pm 4.09$  and  $194 \pm 6.18 \mu\text{m}$ ). All the composite scaffolds present similar porosities, which have no significant difference between each other. The SF/SPI/GO scaffold has the highest porosity ( $87.66 \pm 2.77\%$ ), while the control SF scaffold has the lowest porosity ( $79.32 \pm 1.62\%$ ). The porosities of the SF/SPI, SF/SPI/ $\beta$ -TCP, and SF/SPI/GO/ $\beta$ -TCP scaffolds are ( $82.28 \pm 2.15\%$ ), ( $82.63 \pm 1.04\%$ ), and ( $80.45 \pm 2.04\%$ ), respectively.

**Table 2.** The pore size and porosity of SF-based composite scaffolds.

	SF	SF/SPI	SF/SPI/GO	SF/SPI/ $\beta$ -TCP	SF/SPI/ $\beta$ -TCP/GO
Pore size ( $\mu\text{m}$ )	$117.76 \pm 6.33$	$113.37 \pm 6.33$	$108 \pm 6.33$	$232.53 \pm 4.09$	$194 \pm 6.18$
Porosity (%)	$79.32 \pm 1.62$	$82.28 \pm 2.15$	$87.66 \pm 2.77$	$82.63 \pm 1.04$	$80.45 \pm 2.04$

### 3.1.2. Mechanical Properties of the SF/SPI-Based Composite Scaffolds

Mechanical properties of the composite scaffolds are shown in Figure 3. The SF scaffold had the lowest compressive strength ( $0.333 \pm 0.085$  MPa). The compressive strengths of the SF/SPI and SF/SPI/GO scaffolds were  $0.432 \pm 0.072$  and  $0.660 \pm 0.022$  MPa, respectively. The compressive strengths of the SF/SPI/ $\beta$ -TCP and SF/SPI/GO/ $\beta$ -TCP scaffolds were  $1.020 \pm 0.122$  MPa and  $0.802 \pm 0.065$  MPa respectively, which were significantly higher than those of the SF-based scaffolds without  $\beta$ -TCP particles ( $p < 0.05$ ).

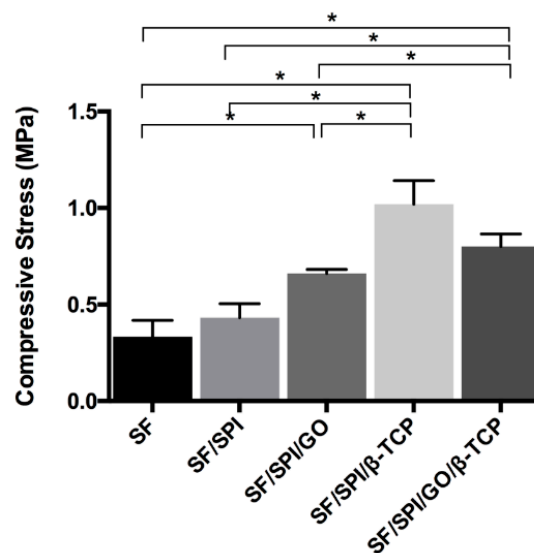


**Figure 3.** Mechanical properties of the SF/SPI-based composite scaffolds. Statistical significance relative to each group: \*  $p < 0.05$ .

### 3.1.3. Chemical Constituents of the SF/SPI-Based Composite Scaffolds

Figure 4 shows the XRD pattern of the SF/SPI-based composite scaffolds. A weak peak locates at  $9.7^\circ$  and  $20.2^\circ$  corresponding to the  $\beta$ -sheet crystalline structure (silk-II structure) of native SF. However, the weak signal of SF around  $20^\circ$  is overlapped by the signal of SPI in the hybrid scaffolds, which is the characteristic diffraction peaks at  $19.7^\circ$  in the SPI XRD pattern corresponding to the  $\beta$ -sheet structures of the protein secondary conformation. When  $\beta$ -TCP nanoparticles are incorporated, the peaks occur at  $31.0^\circ$  and  $34.3^\circ$ , and match the standard  $\beta$ -TCP JCPDS 09-0169 card. The characteristic peak (001) of GO at  $10.2^\circ$  is not observed in GO-incorporated scaffolds in the present study, probably because of the low content or the overlap position of the SF characteristic peak at  $9.7^\circ$ .

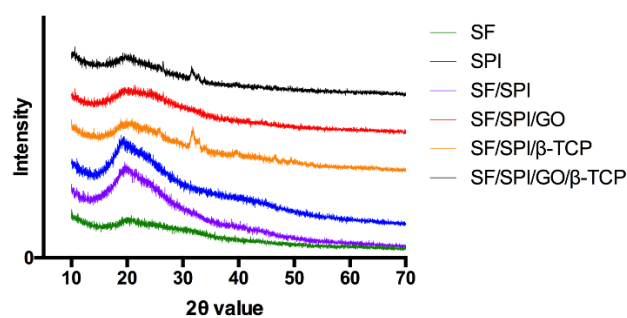


**Figure 4.** X-ray diffraction (XRD) patterns of the SF/SPI-based composite scaffolds.

ATR-FTIR patterns of the SF/SPI-based composite scaffolds are shown in Figure 5. All of the scaffolds exhibit characteristic peaks at  $1612\text{ cm}^{-1}$  (C=O stretching vibration),  $1513\text{ cm}^{-1}$  (N-H bending), and  $1298\text{ cm}^{-1}$  (C-H and N-H stretching), which could be ascribed to amide I, amide II, and amide III

of SF respectively [28,29]. Also, the ATR-FTIR spectrum of SPI displays similar characteristic peaks ( $1630\text{ cm}^{-1}$ ,  $1530\text{ cm}^{-1}$ , and  $1230\text{ cm}^{-1}$ ) to that of SF based on several literatures, which are difficult to distinguish in hybrid scaffolds [30]. Hydroxy groups (-OHs) of SF appear at  $3260\text{ cm}^{-1}$ , the N-H stretching vibration of SPI is at  $3460\text{ cm}^{-1}$ . When SF is mixed with SPI, the hybrid characteristic peak becomes obviously broad, and moves to lower adsorption band ( $3400\text{ cm}^{-1}$ ), indicating that the two proteins are not only physically blended together, but interacted through hydrogen bonding. The SF/SPI/ $\beta$ -TCP and SF/SPI/GO/ $\beta$ -TCP scaffolds exhibit the characteristic peak at  $660\text{ cm}^{-1}$ , which attributes to  $\text{PO}_4^{3-}$  groups [29,31,32]. The addition of GO enhances the intensity of -OH groups ( $3200\text{ cm}^{-1}$  to  $3700\text{ cm}^{-1}$ ) with broader band, representing the intermolecular hydrogen bonding in the scaffold. The absorption peaks at  $1732\text{ cm}^{-1}$  and  $1628\text{ cm}^{-1}$  are ascribed to the C=O stretching vibration of carboxyl groups and C=C stretching of  $\text{sp}^2$  hybridized crystal structures of graphite, respectively [33]. Only the adsorption peak of GO at  $1732\text{ cm}^{-1}$  is detected in the composite scaffolds, while the adsorption peak at  $1628\text{ cm}^{-1}$  is overlapped by the adsorption band of amide I.

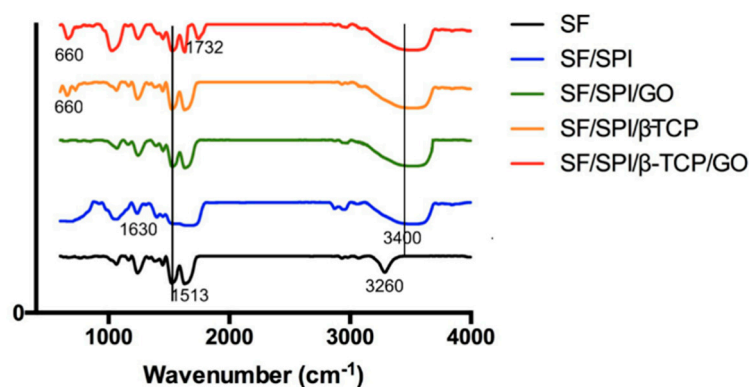


Figure 5. ATR-FTIR patterns of the SF/SPI-based composite scaffolds.

Water adsorption behaviors of the SF/SPI composite scaffolds are shown in Figure 6. All of the scaffolds display good water adsorption behaviors in 24 h. The control SF scaffold rapidly reaches the swelling ratio of 1465% at 3 h, and tends to be constant, i.e., 1661% at 24 h. The scaffolds SPI, SF/SPI exhibit a rapid increase up to 2346% after 3 h immersion, and become stable (2321%) until 24 h. The SF/SPI/GO scaffold has the highest swelling ratio (i.e., 2668%) at 4 h, slightly decreases to 2540% at 12 h, and finally reaches 2560% at 24 h. The water adsorption ratios of the SF/SPI/ $\beta$ -TCP and SF/SPI/GO/ $\beta$ -TCP scaffolds initially have a slow increase, when compared with pure SF scaffold. After 4 h immersion, the SF/SPI/ $\beta$ -TCP and SF/SPI/GO/ $\beta$ -TCP scaffolds exhibit a rapid increase up to 1508% and 1569%, and approximately keep 1450% and 1856% at 24 h, respectively. The water adsorption ratios of the SF/SPI and SF/SPI/GO scaffolds are significantly higher than those of the SF and SF/SPI/ $\beta$ -TCP scaffolds at 24 h ( $p < 0.05$ ).

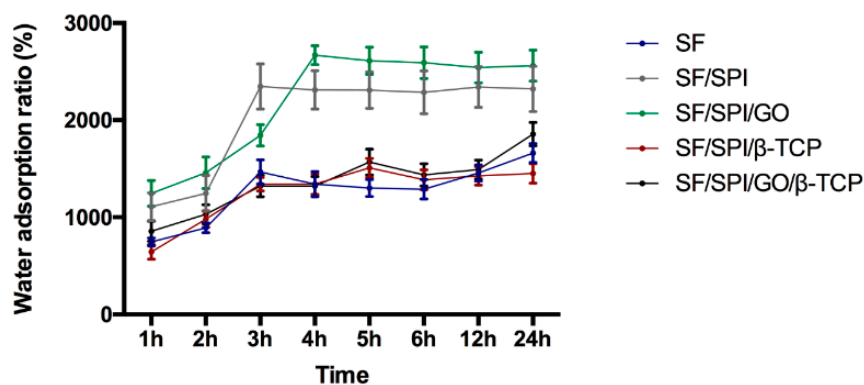
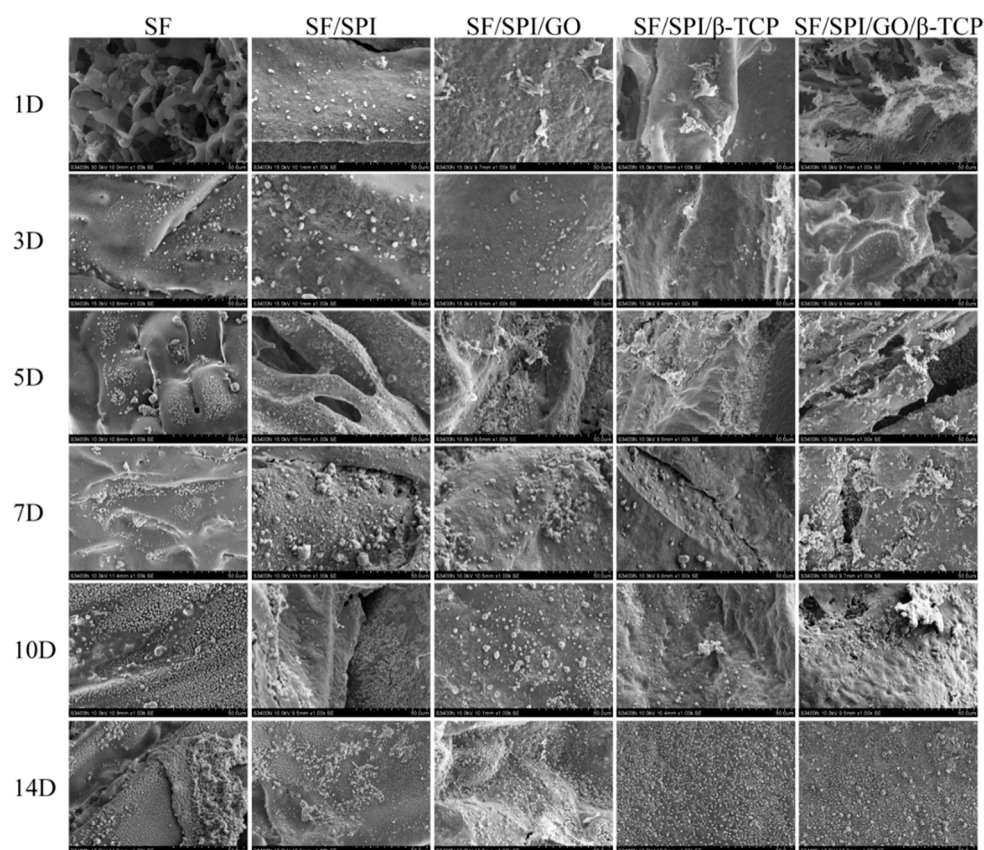


Figure 6. Water adsorption behaviors of the SF/SPI-based composite scaffolds in 24 h.



### 3.2. In Vitro Biomineralization Capability of the SF/SPI-Based Composite Scaffolds

Biomineralization capability is an essential factor to promote bone-binding competence for bone repair materials. The surface morphologies of the Ca-P minerals on the composite scaffolds are confirmed by the SEM images (Figure 7) and XRD analyses (Figure 8). Generally, no mineral deposition is found on each scaffold until the 3rd day. After incubation in the SBF solution for 5 days, lamellar nanocrystals are observed on the surface of each scaffold. Obviously, there are more mineral deposition on the surface of each scaffold with the increased immersion time. It is interesting that the minerals are sparsely and randomly distributed on the SF scaffold, while there are denser mineral aggregations on the scaffolds with the presence of GO or  $\beta$ -TCP nanoparticles. Besides, the SF/SPI/GO scaffold displays more lamellar nanocrystals, when compared with SF and SF/SPI scaffolds, indicating the nanocrystal deposition is increased in the presence of GO. With the incorporation of  $\beta$ -TCP nanoparticles, there are more nanocrystals formed on the surface of the SF/SPI/ $\beta$ -TCP scaffold. However, no differences are observed between the SF/SPI/ $\beta$ -TCP and SF/SPI/GO/ $\beta$ -TCP scaffolds via SEM.



**Figure 7.** Field emission scanning electron microscope (FESEM) photographs of the SF/SPI-based composite scaffolds after immersing into simulated body fluid (SBF) solution at different time points.

As shown in Figure 8, the XRD patterns after incubation in SBF solution for 14 days display the characteristic peaks corresponding to apatite at  $26.0^\circ$  (002) and  $31.77^\circ$  (211) (JCPDS 9432 card), which confirm the nucleation of hydroxyapatite (HA) in all the samples. Extremely weak peak at  $26.0^\circ$  is observed on SF scaffold, indicating small amount and low crystallinity of apatite formed. The SF/SPI scaffold demonstrates a similar extent of mineralization as that of the SF/SPI/GO. Additionally, the narrow peaks at  $26^\circ$  and  $31^\circ$  with strongest intensities, as well as the particular peak at  $54^\circ$  on SF/SPI/GO/ $\beta$ -TCP scaffold illustrate that there are more HA particles with higher crystallinity and larger size deposited on the SF/SPI/GO/ $\beta$ -TCP scaffold.

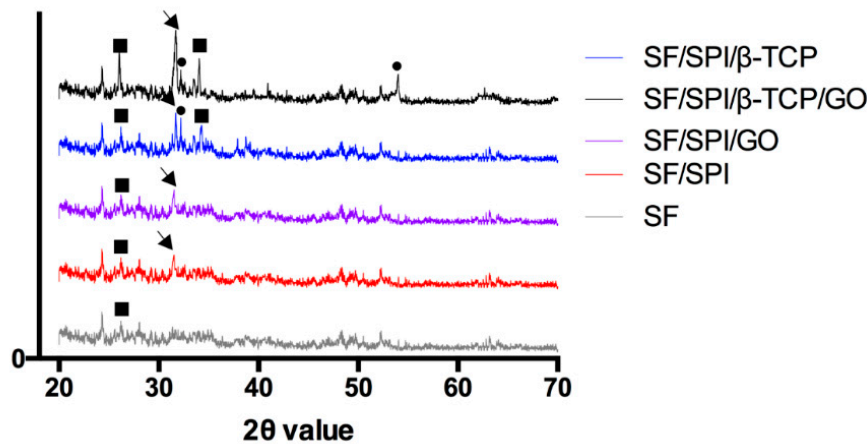


**Figure 8.** XRD patterns of the SF/SPI-based composite scaffolds after immersing into SBF solution for 14 days (circle refers to hydroxyapatite; arrow refers to apatite; square refers to  $\beta$ -TCP).

### 3.3. Morphologies and Proliferation of BMSCs on the SF/SPI-Based Composite Scaffolds

Cell morphologies of BMSCs on the SF/SPI-based composite scaffolds are observed at 48 h using both SEM and confocal microscopy. As shown in Figure 9, there are elongated spindle-shaped cells well adhered onto the surface of the SF/SPI/GO, SF/SPI/ $\beta$ -TCP, and SF/SPI/GO/ $\beta$ -TCP scaffolds, while there are less cells on the SF and SF/SPI scaffolds. Obviously, cells on the SF/SPI/GO/ $\beta$ -TCP scaffold exhibit the most spreading and adhesive morphologies.

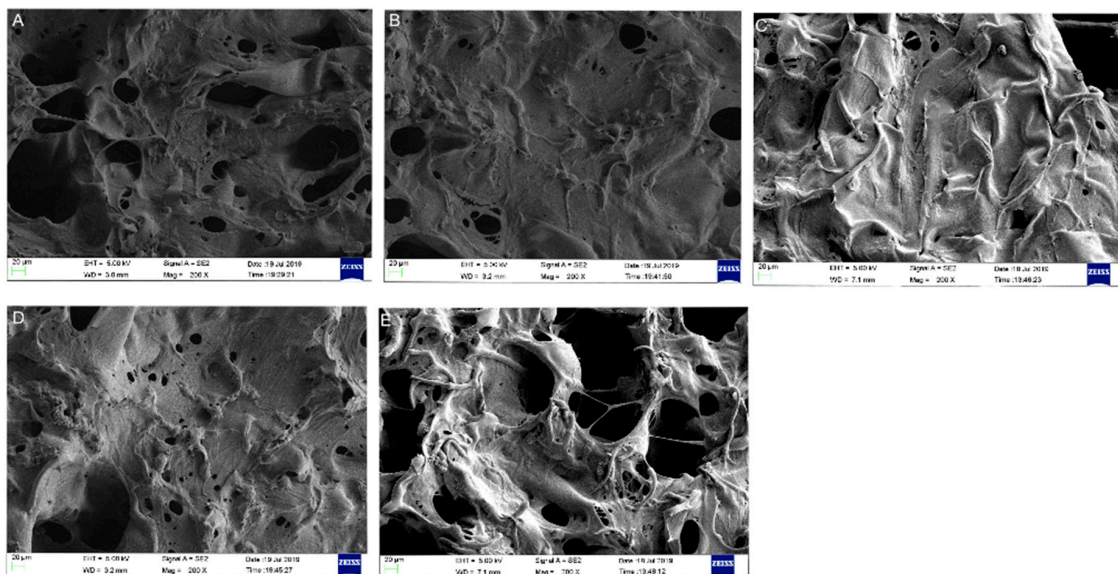


**Figure 9.** Scanning electron microscope (SEM) photographs of bone marrow mesenchymal stem cells (BMSCs) seeding on the SF/SPI-based composite scaffolds ((A): SF; (B): SF/SPI; (C): SF/SPI/GO; (D): SF/SPI/ $\beta$ -TCP; (E): SF/SPI/GO/ $\beta$ -TCP).

BMSC proliferation rate on the composite scaffolds is investigated using CCK-8 kit on 1, 3, 5, and 7 days. As shown in Figure 10, cell viability on the SF scaffold decreases slightly with time increasing, which remains approximately 80%, while cell viabilities increase on the other four scaffolds with increasing time. This may be due to the reason that there are not sufficient receptors on the surface of the SF scaffold for cell adhesion and spreading. Cell viabilities on the SF/SPI and SF/SPI/GO scaffolds remained the same as that of the 1st day, which was significantly higher than those of the other three scaffolds ( $p < 0.05$ ). No differences were found on each scaffold on the 3rd day. Since the 5th day, cell viabilities on the SF and SF/SPI/ $\beta$ -TCP scaffolds slightly decrease. Meanwhile, cell viabilities on the

SF/SPI/GO and SF/SPI/GO/ $\beta$ -TCP scaffolds exhibit the highest levels, which are significantly higher than the other three groups ( $p < 0.05$ ). On the 7th day, the SF/SPI/GO and SF/SPI/GO/ $\beta$ -TCP scaffolds still exhibit the highest cell viabilities ( $p < 0.05$ ).

These results are consistent with the confocal images as shown in Figure 11, where BMSCs behave totally different on the SF/SPI-based scaffolds. On the pure SF and SF/SPI scaffolds the nuclei are blue and clear but the cytoplasm and cytoskeleton are sparse and vague (Figure 11A,B). On the SF/SPI/GO scaffold, the numbers of cells are obviously increased with many divisions (i.e., double nuclei, Figure 11C). Cell-cell interactions are extremely active with stretched pseudopodia. On the SF/SPI/ $\beta$ -TCP scaffold, some cells are at division states with spread cytoskeleton (Figure 11D). While on the SF/SPI/GO/ $\beta$ -TCP scaffold, cell activities attend the highest with bright blue nuclei and fibrous orange cytoskeleton (Figure 11E). There are more elongated and spindle cell shapes on the composite scaffolds with  $\beta$ -TCP or GO nanoparticles, when compared with the pure SF and SF/SPI scaffolds.

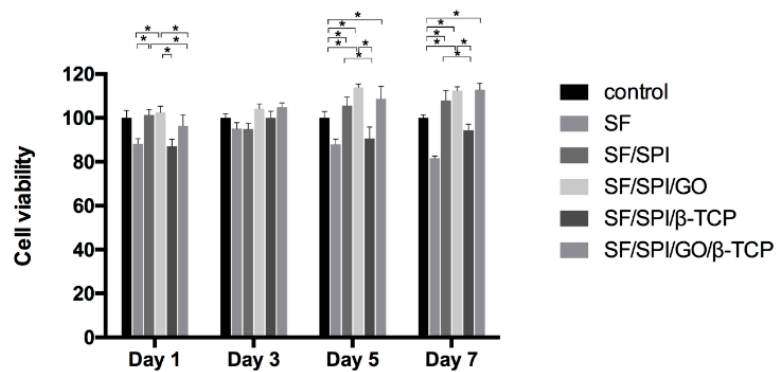


**Figure 10.** Proliferation of BMSCs on the SF/SPI-based scaffolds on day 1, 3, 5, and 7. Statistical significance relative to each group: \*  $p < 0.05$ .

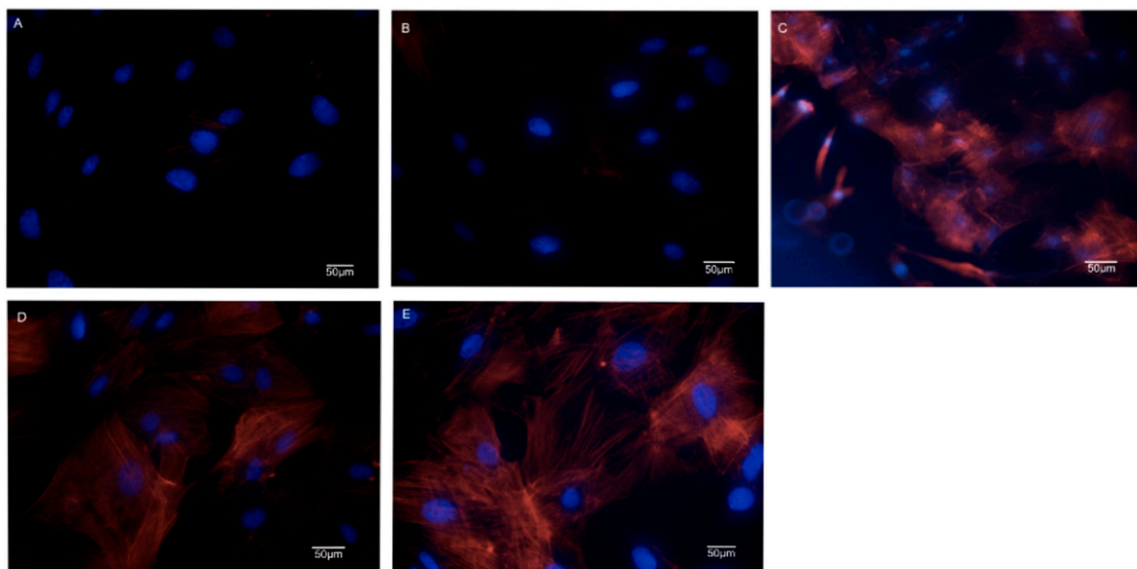


**Figure 11.** Confocal images of BMSCs on the SF/SPI-based scaffolds ((A): SF; (B): SF/SPI; (C): SF/SPI/GO; (D): SF/SPI/ $\beta$ -TCP; (E): SF/SPI/GO/ $\beta$ -TCP).

### 3.4. ALP Activities of BMSCs on the SF/SPI-Based Composite Scaffolds

ALP is widely used as a maker of early differentiation of MSCs. ALP activities of BMSCs on different scaffolds on day 1, 3, 5, and 7 are shown in Figure 12. On the 1st day, the SF/SPI/ $\beta$ -TCP group has a significantly higher ALP level than the other four scaffolds ( $p < 0.05$ ). No significant differences are found on the ALP activity between the SF, SF/SPI, SF/SPI/GO, and SF/SPI/GO/ $\beta$ -TCP groups. ALP

activities on all scaffolds except the SF/SPI/GO group slightly decrease on the 3rd day. ALP activities almost keep the same for the SF/SPI/GO and SF/SPI/ $\beta$ -TCP groups, which are significantly higher than those of the other three groups ( $p < 0.05$ ). ALP activities on all scaffolds rapidly increase on the 5th day and decrease on the 7th day. On the 5th day, the SF/SPI/GO/ $\beta$ -TCP has the highest ALP activity, which is almost two-fold higher than that of the SF/SPI/GO group ( $p < 0.05$ ). The SF/SPI/GO group has a significantly higher ALP level than the SF, SF/SPI, and SF/SPI/ $\beta$ -TCP groups ( $p < 0.05$ ), while no differences are found on ALP level between the SF/SPI and SF/SPI/ $\beta$ -TCP groups. On the 7th day, ALP activities of all the groups almost keep at the same level without any differences.

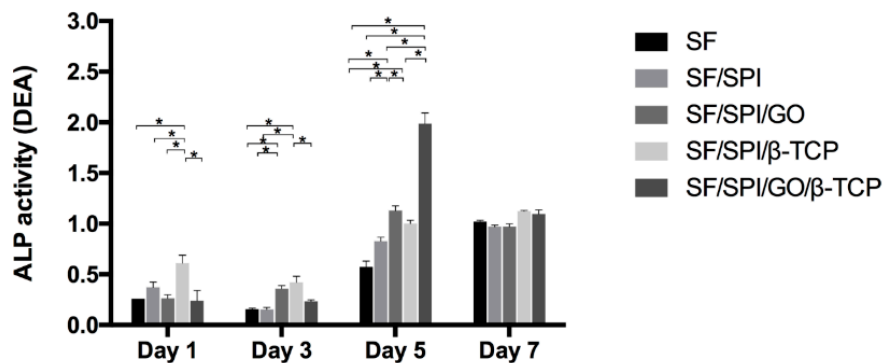


**Figure 12.** ALP activities of BMSCs on the SF/SPI-based composite scaffolds on day 1, 3, 5 and 7. Statistical significance relative to each group: \*  $p < 0.05$ .

### 3.5. Osteogenesis-Related Gene Expression of BMSCs on the SF/SPI-Based Composite Scaffolds

Runx 2 is known as an osteogenic transcriptional factor, as well as an early marker of osteogenic differentiation. Figure 13 displays the Runx 2 mRNA level of BMSCs cultured on the SF/SPI-based composite scaffolds. On the 7th day, the SF/SPI/GO scaffold has the highest Runx2 level, which is significantly higher than those of the SF and SF/SPI/ $\beta$ -TCP scaffolds ( $p < 0.05$ ). Runx 2 level on the SF/SPI/ $\beta$ -TCP/GO scaffold is slightly lower than that of the SF/SPI/GO scaffold, and significantly higher than that of the SF scaffold ( $p < 0.05$ ). After 14 days of culture, the Runx 2 level slightly decreases on the SF and SF/SPI scaffolds. Interestingly, Runx 2 level on the SF/SPI/GO/ $\beta$ -TCP scaffold is up-regulated the most, which is significantly higher than those of the SF, SF/SPI, and SF/SPI/ $\beta$ -TCP scaffolds ( $p < 0.05$ ). Additionally, the SF/SPI/GO group has a significantly higher Runx 2 level, when compared with the SF and SF/SPI groups ( $p < 0.05$ ).

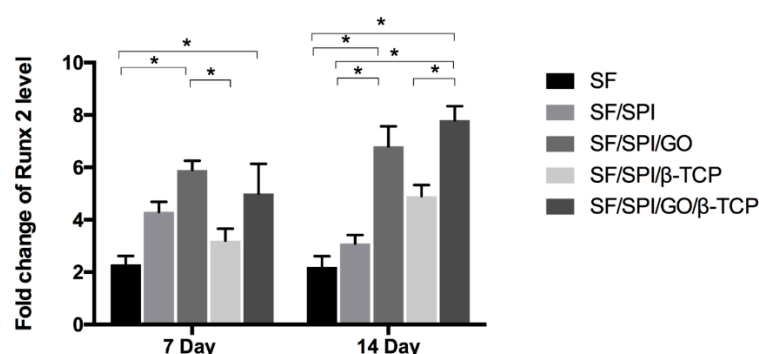


**Figure 13.** Runx 2 mRNA expression of BMSCs on the SF/SPI-based composite scaffolds on day 7 and 14. Statistical significance relative to each group: \*  $p < 0.05$ .

Osteocalcin (OC), a specific protein related to osteoblasts, has been widely used as a late marker of osteogenic differentiation. As shown in Figure 14, all scaffolds have an increasing OC level with time increasing. The SF/SPI/GO/ $\beta$ -TCP group exhibits the highest OC level on the 7th day, which is significantly higher than that of the SF group ( $p < 0.05$ ). OC level of BMSCs on the SF/SPI/GO

group is significantly higher than that of the SF and SF/SPI/ $\beta$ -TCP groups on the 14th day ( $p < 0.05$ ). No differences are found on OC level between the SF, SF/SPI, and SF/SPI/GO groups.

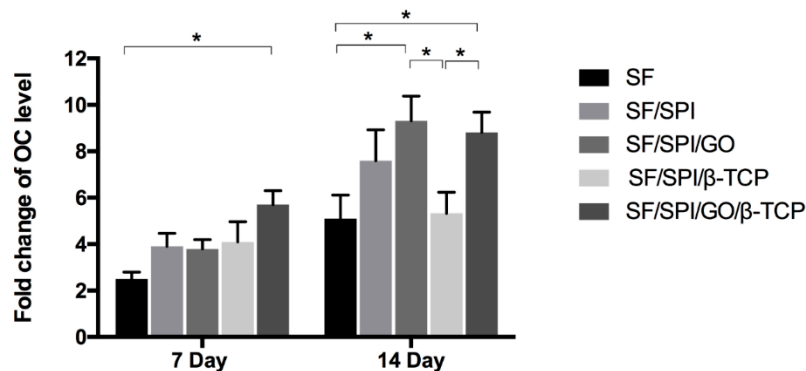


**Figure 14.** OC mRNA expression of BMSCs on the SF/SPI-based composite scaffolds on day 7 and 14. Statistical significance relative to each group: \*  $p < 0.05$ .

Collagen type I (Col I) is the main component in the composition of ECMs. It is an important marker protein in osteogenesis. As shown in Figure 15, the SF/SPI, SF/SPI/ $\beta$ -TCP, and SF/SPI/GO/ $\beta$ -TCP groups have an increasing Col I level with time increasing, while Col I level on the SF and SF/SPI/GO groups decreases slightly from the day 7 to 14. On the 7th day, there are significantly increased OC levels on the SF/SPI/GO/ $\beta$ -TCP and SF/SPI/GO scaffolds compared with the SF scaffold ( $p < 0.05$ ). In addition, the Col I level reaches the highest value on the SF/SPI/GO/ $\beta$ -TCP scaffold on the 14th day, that is considerably higher than those of the other four scaffolds ( $p < 0.05$ ). OC levels of BMSCs on the SF/SPI/GO and SF/SPI/ $\beta$ -TCP scaffolds are significantly higher than those of the SF and SF/SPI scaffolds ( $p < 0.05$ ).

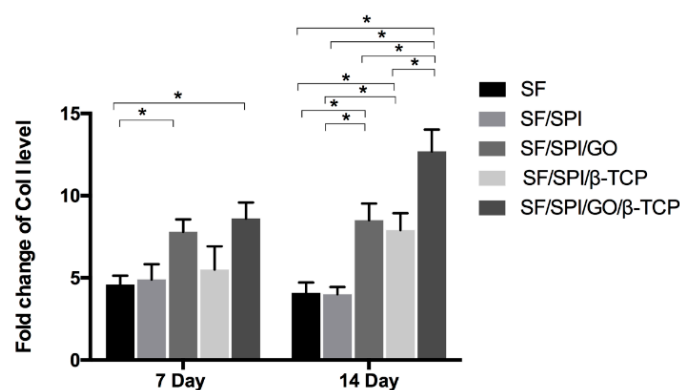


**Figure 15.** Col I mRNA expression of BMSCs on the SF/SPI-based composite scaffolds on day 7 and 14. Statistical significance relative to each group: \*  $p < 0.05$ .

#### 4. Discussion

SF and SPI are both natural polymers that have been widely used as scaffolds for tissue engineering and regenerative medicine [34–37]. However, there are many limitations for these polymers to be used as bone repair scaffolds because of the poor mechanical properties and insufficient osteoinductive capabilities.

It is generally accepted that the pore geometry in a scaffold, including pore size, pore shape, porosity, and pore interconnecting pattern, plays an important role in cell adhesion, proliferation, and migration as well as tissue ingrowth [38,39]. Larger pore sizes favor tissue ingrowth and vascularization, resulting in better osteogenesis, while smaller pores lead to osteochondral ossification [40]. An ideal bone

scaffold should have 100–600  $\mu\text{m}$  pore size with 60–80% porosity to provide enough space for cell migration, tissue ingrowth, and vascularization.

In this study, all the SF/SPI scaffolds fabricated through freeze-drying have an average pore size of more than 100  $\mu\text{m}$  and proper porosities. With these pores, the amount of the incorporated  $\beta$ -TCP and GO nanoparticles can be significantly increased, which subsequently affects the hydrophobicity of the whole scaffolds [29,31]. When the  $\beta$ -TCP and GO nanoparticles appear on the surface of the pore walls, there form flake-like structures with sharp pore edges, which increase the surface roughness. The good dispersion of the nanoparticles of  $\beta$ -TCP and GO and the altered surface properties could be helpful to enhance cell behaviors [36,41,42].

It is considered that appropriate mechanical properties are necessary for bone tissue engineering. In the present study, the single SF scaffold has low mechanical properties (0.33 MPa), while the SF/SPI composite scaffold holds significantly increased compressive strength (0.42 MPa). This could be explained by the effect of chemical-crosslinked polymer chains. Furthermore, the reinforcement of GO increases the compressive strength value of the scaffold to 0.66 MPa. It could be due to the formation of hydrogen bonds among -OH and -COOH functional groups on the GO surface and hydroxyl groups in the SF or SPI molecules [18,43]. The incorporation of  $\beta$ -TCP particles can obviously enhance the mechanical properties of the SF/SPI scaffolds. It is noted that the compressive strength (i.e.,  $1.020 \pm 0.122$  MPa) of the SF/SPI/ $\beta$ -TCP scaffold is similar to that of the natural trabecular bone (1–7 MPa) [44]. This is beneficial for bone repair without the help of extra mechanical support [45–49].

It is generally accepted that in vitro biomineralization of a porous scaffold through a layer of an apatite formation over the scaffold surface could provide direct integration between host bone and the bioactive mineral layers, thereby accelerating bone healing [27]. The SBF solution is often used to imitate a physiological environment, which can nucleate bone-like HA on bone repair materials [50]. The HA particles formed on the scaffolds can be increased with the increasing incubation time. Previous studies demonstrated the biomineralization process was influenced by the functional groups (i.e., amino, carboxyl and hydroxyl group), surface charge, and surface morphology [51,52].

In the present study, both SF and SF/SPI scaffolds lead to a similar HA nucleation, which could be explained by the fact that both SF and SPI molecules have similar amino acid compositions. Interestingly, with the incorporation of GO with enriched functional groups, no differences are found on the intensity and sharp degrees of the XRD peaks of the SF/SPI and SF/SPI/GO scaffolds (Figure 5), indicating the types of functional groups are not the decisive factor that affected the biomineralization processes [24,53–57]. However, more characteristic peaks with considerably greater intensities are found in the presence of  $\beta$ -TCP, indicating a greater extent of mineralization on the SF/SPI/ $\beta$ -TCP and SF/SPI/GO/ $\beta$ -TCP scaffolds. It is speculated that more calcium ions ( $\text{Ca}^{2+}$ ) released from the  $\beta$ -TCP nanoparticles could incorporate with the functional groups through electrostatic interactions, subsequently formed minerals with phosphate groups ( $\text{PO}_4^{-3}$ ), and facilitated the nucleation and growth of HA crystals on the surface of the scaffolds [58]. Additionally, the rough flake-like morphologies on the  $\beta$ -TCP-incorporated scaffolds are also attributed to the enhanced HA nucleation [59]. Thus, along with the larger specific area of GO, the SF/SPI/GO/ $\beta$ -TCP scaffold exhibits the most biomineralization capability in this study.

Some researchers suggested that the initial cell adhesion and proliferation states at material-tissue interface play a crucial role in the early stage of bone formation. In the present study, BMSCs are well adhered on all the scaffolds though SEM and confocal observation. Compared to pure SF and SF/SPI scaffolds, the incorporation of  $\beta$ -TCP and GO nanoparticles enhances the cell adhesive capability. Along with CCK-8 results, the simultaneous incorporation of  $\beta$ -TCP and GO nanoparticles into SF/SPI scaffolds has a better cell morphology and viability compared to GO or  $\beta$ -TCP alone. GO nanoparticles provide larger specific surface area, which facilitate more cell adherence onto the scaffold surface with well-spread morphologies. Cell behaviors can also be influenced by the hydrophilicity of the scaffold surface [60–64]. The hydrophilic property of GO-incorporated SF/SPI scaffolds is likely responsible for the increasing swell ratio. Therefore, the enhancement of water adsorption behaviors on GO-incorporated composite scaffolds facilitates the adhesion and proliferation of the BMSCs [65–69].

The osteoinductive ability of composite scaffolds are investigated using ALP activities, through measuring the Runx 2, OC and Col I expression levels of BMSCs. It is found that the incorporation of  $\beta$ -TCP and GO nanoparticles into the composite scaffolds has significantly increased the mRNA levels of osteogenesis-related genes, indicating the synergistic effect in the osteogenesis of BMSCs via incorporating  $\beta$ -TCP and GO nanoparticles. It was reported that the surface characteristics of GO could influence the molecular pathway of stem cells [70]. Nevertheless, the regulatory mechanism of  $\beta$ -TCP and GO nanoparticles on osteogenesis remains poorly understood. In the present study, most of the GO flakes are covered by  $\beta$ -TCP particles, and formed GO- $\beta$ -TCP complexes on the pore edges, which are beneficial for the direct absorption of molecules. The enhanced osteogenic differentiation capability might be partly due to the increased interaction between the intracellular focal adhesion complexes and GO- $\beta$ -TCP structures [71]. Partly, the incorporation of  $\beta$ -TCP has increased the mechanical properties, which could induce an improved mechanotransduction effect to regulate cells differentiation. Actually, our results are in accordance with previous studies, which indicate that novel GO-CaP nanocomposites could synthetically promote osteogenesis of MSCs and further enhance calcium deposition by osteoblasts [72,73]. As discussed above, the simultaneous incorporation of  $\beta$ -TCP and GO nanoparticles facilitates biomineralization, and subsequently provides a biomimetic environment for BMSC osteogenesis. Further elucidation of the underlying molecular mechanism and signal pathway related BMSCs osteogenesis through  $\beta$ -TCP and GO nanoparticles will be conducted in the next study.

## 5. Conclusions

In present study, a series of SF/SPI-based composite scaffolds are fabricated by incorporating  $\beta$ -TCP and GO nanoparticles individually or simultaneously. The incorporation of  $\beta$ -TCP has significantly increased the pore size and compressive strength, while the incorporation of GO has enhanced water adsorption behaviors of the composite scaffolds. More specifically, simultaneous incorporation of  $\beta$ -TCP and GO particles has facilitated biomineralization with an obvious synergistic effect on improving the adhesion, proliferation, and osteogenic differentiation of the BMSCs. In another word, the cooperation of GO and  $\beta$ -TCP nanoparticles possesses synergistic effect in osteogenesis of BMSCs compared with GO or  $\beta$ -TCP nanoparticle alone. It is expected that the GO and  $\beta$ -TCP nanoparticle incorporated SF/SPI scaffolds will be good candidates for future bone tissue regeneration.

**Author Contributions:** Original draft preparation, F.L.; allocation, supplement, and editing, X.W.; methodology, C.L. and J.L.; investigation, B.Z.; data curation, J.H.; supervision, C.C.; project administration, I.-s.L. and Y.L.; funding acquisition, Y.L. and X.W. All authors have read and agreed to the published version of the manuscript.

**Funding:** This work was supported by the National Nature Science Foundation of China (NSFC) (Nos. 81571832, 81701033, 81271665), the Key Research & Development Project of Liaoning Province (Nos. 2018225082, 2019JH8/10300015), Natural Science Foundation of Zhejiang Province (grant number LY20E010006), the 2017 Discipline Promotion Project of China Medical University (CMU) (No. 3110117049), and the 2018 Scientist Partners of China Medical University (CMU) and Shenyang Branch of Chinese Academy of Sciences (CAS) (No. HZHB2018013).

**Conflicts of Interest:** The authors declare no conflict of interest. The founding sponsors had no role in the design of the study; in the collection, analyses, or interpretation of data; in the writing of the manuscript, and in the decision to publish the results.

## References

1. Tatara, A.M.; Shah, S.R.; Demian, N.; Ho, T.; Shum, J.; van den Beucken, J.J.J.P.; Jansen, J.A.; Wong, M.E.; Mikos, A.G. Reconstruction of large mandibular defects using autologous tissues generated from in vivo bioreactors. *Acta Biomater.* **2016**, *45*, 72–84. [[CrossRef](#)] [[PubMed](#)]
2. Hosseinpour, S.; Ghazizadeh Ahsaie, M.; Rezai Rad, M.; Baghani, M.T.; Motamedian, S.R.; Khojasteh, A. Application of selected scaffolds for bone tissue engineering: A systematic review. *Oral Maxillofac. Surg.* **2017**, *21*, 109–129. [[CrossRef](#)] [[PubMed](#)]

3. Thibaudeau, L.; Taubenberger, A.V.; Holzapfel, B.M.; Quent, V.M.; Fuehrmann, T.; Hesami, P.; Brown, T.D.; Dalton, P.D.; Power, C.A.; Hollier, B.G.; et al. A tissue-engineered humanized xenograft model of human breast cancer metastasis to bone. *Dis. Model. Mech.* **2014**, *7*, 299–309. [[CrossRef](#)] [[PubMed](#)]
4. Place, E.S.; Evans, N.D.; Stevens, M.M. Complexity in biomaterials for tissue engineering. *Nat. Mater.* **2009**, *8*, 457–470. [[CrossRef](#)]
5. Gu, Y.; Bai, Y.; Zhang, D. Osteogenic stimulation of human dental pulp stem cells with a novel gelatin-hydroxyapatite-tricalcium phosphate scaffold. *J. Biomed. Mater. Res. A* **2018**, *106*, 1851–1861. [[CrossRef](#)]
6. Kundu, B.; Rajkhowa, R.; Kundu, S.C.; Wang, X. Silk fibroin biomaterials for tissue regenerations. *Adv. Drug Deliv. Rev.* **2013**, *65*, 457–470. [[CrossRef](#)]
7. Jin, H.-J.; Chen, J.; Karageorgiou, V.; Altman, G.H.; Kaplan, D.L. Human bone marrow stromal cell responses on electrospun silk fibroin mats. *Biomaterials* **2004**, *25*, 1039–1047. [[CrossRef](#)]
8. Liu, F.; Chen, Q.; Liu, C.; Ao, Q.; Tian, X.; Fan, J.; Tong, H.; Wang, X. Natural polymers for organ 3D bioprinting. *Polymers* **2018**, *10*, 1278. [[CrossRef](#)]
9. Gaffney-Stomberg, E.; Cao, J.J.; Lin, G.G.; Wulff, C.R.; Murphy, N.E.; Young, A.J.; McClung, J.P.; Pasiakos, S.M. Dietary protein level and source differentially affect bone metabolism, strength, and intestinal calcium transporter expression during ad libitum and food-restricted conditions in male rats. *J. Nutr.* **2014**, *144*, 821–829. [[CrossRef](#)]
10. Dirkes, R.K.; Richard, M.W.; Meers, G.M.; Butteiger, D.N.; Krul, E.S.; Thyfault, J.P.; Rector, R.S.; Hinton, P.S. Soy protein isolate suppresses bone resorption and improves trabecular microarchitecture in spontaneously hyperphagic, rapidly growing male OLETF rats. *Curr. Dev. Nutr.* **2018**, *2*, nzy010. [[CrossRef](#)]
11. Chen, J.-R.; Lazarenko, O.P.; Blackburn, M.L.; Badger, T.M.; Ronis, M.J.J. Soy Protein Isolate Inhibits High Fat Diet-Induced Senescence Pathways in Osteoblasts to Maintain Bone Acquisition in Male Rats. *Endocrinology* **2015**, *156*, 475–487. [[CrossRef](#)]
12. Luo, Y.; Shen, H.; Fang, Y.; Cao, Y.; Huang, J.; Zhang, M.; Dai, J.; Shi, X.; Zhang, Z. Enhanced proliferation and osteogenic differentiation of mesenchymal stem cells on graphene oxide-incorporated electrospun poly(lactic-co-glycolic acid) nanofibrous mats. *ACS Appl. Mater. Interfaces* **2015**, *7*, 6331–6339. [[CrossRef](#)]
13. Nayak, T.R.; Andersen, H.; Makam, V.S.; Khaw, C.; Bae, S.; Xu, X.; Ee, P.-L.R.; Ahn, J.-H.; Hong, B.H.; Pastorin, G.; et al. Graphene for controlled and accelerated osteogenic differentiation of human mesenchymal stem cells. *ACS Nano* **2011**, *5*, 4670–4678. [[CrossRef](#)]
14. Guo, W.; Wang, S.; Yu, X.; Qiu, J.; Li, J.; Tang, W.; Li, Z.; Mou, X.; Liu, H.; Wang, Z. Construction of a 3D rGO-collagen hybrid scaffold for enhancement of the neural differentiation of mesenchymal stem cells. *Nanoscale* **2016**, *8*, 1897–1904. [[CrossRef](#)]
15. Wen, J.H.; Vincent, L.G.; Fuhrmann, A.; Choi, Y.S.; Hribar, K.C.; Taylor-Weiner, H.; Chen, S.; Engler, A.J. Interplay of matrix stiffness and protein tethering in stem cell differentiation. *Nat. Mater.* **2014**, *13*, 979–987. [[CrossRef](#)]
16. Mohammadrezaei, D.; Golzar, H.; Rezai Rad, M.; Omid, M.; Rashedi, H.; Yazdian, F.; Khojasteh, A.; Tayebi, L. In vitro effect of graphene structures as an osteoinductive factor in bone tissue engineering: A systematic review. *J. Biomed. Mater. Res. A* **2018**, *106*, 2284–2343. [[CrossRef](#)]
17. Shin, S.R.; Li, Y.-C.; Jang, H.L.; Khoshakhlagh, P.; Akbari, M.; Nasajpour, A.; Zhang, Y.S.; Tamayol, A.; Khademhosseini, A. Graphene-based materials for tissue engineering. *Adv. Drug Deliv. Rev.* **2016**, *105*, 255–274. [[CrossRef](#)]
18. Kolanthai, E.; Sindu, P.A.; Khajuria, D.K.; Veerla, S.C.; Kuppaswamy, D.; Catalani, L.H.; Mahapatra, D.R. Graphene oxide—a tool for the preparation of chemically crosslinking free alginate-chitosan-collagen scaffolds for bone tissue engineering. *ACS Appl. Mater. Interfaces* **2018**, *10*, 12441–12452. [[CrossRef](#)]
19. Lee, J.H.; Ryu, M.Y.; Baek, H.-R.; Lee, K.M.; Seo, J.-H.; Lee, H.-K.; Ryu, H.-S. Effects of porous beta-tricalcium phosphate-based ceramics used as an E. coli-derived rhBMP-2 carrier for bone regeneration. *J. Mater. Sci. Mater. Med.* **2013**, *24*, 2117–2127. [[CrossRef](#)]
20. Duan, R.; Barbieri, D.; Luo, X.; Weng, J.; de Bruijn, J.D.; Yuan, H. Submicron-surface structured tricalcium phosphate ceramic enhances the bone regeneration in canine spine environment. *J. Orthop. Res.* **2016**, *34*, 1865–1873. [[CrossRef](#)]
21. Bose, S.; Tarafder, S. Calcium phosphate ceramic systems in growth factor and drug delivery for bone tissue engineering: A review. *Acta Biomater.* **2012**, *8*, 1401–1421. [[CrossRef](#)]



22. Liu, F.; Liu, Y.; Li, X.; Wang, X.; Li, D.; Chung, S.; Chen, C.; Lee, I.-S. Osteogenesis of 3D printed macro-pore size biphasic calcium phosphate scaffold in rabbit calvaria. *J. Biomater. Appl.* **2019**, *33*, 1168–1177. [[CrossRef](#)] [[PubMed](#)]
23. Wu, J.; Zheng, Z.; Li, G.; Kaplan, D.L.; Wang, X. Control of silk microsphere formation using polyethylene glycol (PEG). *Acta Biomater.* **2016**, *39*, 156–168. [[CrossRef](#)]
24. Wang, X.; Li, D.; Wang, W.; Feng, Q.; Cui, F.; Xu, Y.; Song, X.; van der Werf, M. Crosslinked collagen/chitosan matrices for artificial livers. *Biomaterials* **2003**, *24*, 3213–3220. [[CrossRef](#)]
25. Wang, X.; Yan, Y.; Lin, F.; Xiong, Z.; Wu, R.; Zhang, R.; Lu, Q. Preparation and characterization of a collagen/chitosan/heparin matrix for an implantable bioartificial liver. *J. Biomater. Sci. Polym. E* **2005**, *16*, 1063–1080. [[CrossRef](#)]
26. Zhang, X.-Y.; Chen, Y.-P.; Han, J.; Mo, J.; Dong, P.-F.; Zhuo, Y.-H.; Feng, Y. Biocompatible silk fibroin/carboxymethyl chitosan/strontium substituted hydroxyapatite/cellulose nanocrystal composite scaffolds for bone tissue engineering. *Int. J. Biol. Macromol.* **2019**, *136*, 1247–1257. [[CrossRef](#)]
27. Zou, L.; Zhang, Y.; Liu, X.; Chen, J.; Zhang, Q. Biomimetic mineralization on natural and synthetic polymers to prepare hybrid scaffolds for bone tissue engineering. *Colloids Surf. B Biointerfaces* **2019**, *178*, 222–229. [[CrossRef](#)]
28. Deen, I.; Rosei, F. Silk fibroin-derived polypeptides additives to promote hydroxyapatite nucleation in dense collagen hydrogels. *PLoS ONE* **2019**, *14*, e0219429. [[CrossRef](#)]
29. Park, H.J.; Min, K.D.; Lee, M.C.; Kim, S.H.; Lee, O.J.; Ju, H.W.; Moon, B.M.; Lee, J.M.; Park, Y.R.; Kim, D.W.; et al. Fabrication of 3D porous SF/beta-TCP hybrid scaffolds for bone tissue reconstruction. *J. Biomed. Mater. Res. A* **2016**, *104*, 1779–1787. [[CrossRef](#)]
30. Garrido, T.; Etxabide, A.; Guerrero, P.; de la Caba, K. Characterization of agar/soy protein biocomposite films: Effect of agar on the extruded pellets and compression moulded films. *Carbohydr. Polym.* **2016**, *151*, 408–416. [[CrossRef](#)]
31. Lee, D.H.; Tripathy, N.; Shin, J.H.; Song, J.E.; Cha, J.G.; Min, K.D.; Park, C.H.; Khang, G. Enhanced osteogenesis of beta-tricalcium phosphate reinforced silk fibroin scaffold for bone tissue biofabrication. *Int. J. Biol. Macromol.* **2017**, *95*, 14–23. [[CrossRef](#)] [[PubMed](#)]
32. Baheiraei, N.; Nourani, M.R.; Mortazavi, S.M.J.; Movahedin, M.; Eyni, H.; Bagheri, F.; Norahan, M.H. Development of a bioactive porous collagen/beta-tricalcium phosphate bone graft assisting rapid vascularization for bone tissue engineering applications. *J. Biomed. Mater. Res. A* **2018**, *106*, 73–85. [[CrossRef](#)] [[PubMed](#)]
33. Shamekhi, M.A.; Mirzadeh, H.; Mahdavi, H.; Rabiee, A.; Mohebbi-Kalhari, D.; Baghaban Eslaminejad, M. Graphene oxide containing chitosan scaffolds for cartilage tissue engineering. *Int. J. Biol. Macromol.* **2019**, *127*, 396–405. [[CrossRef](#)] [[PubMed](#)]
34. Yan, Y.; Cheng, B.; Chen, K.; Cui, W.; Qi, J.; Li, X.; Deng, L. Enhanced osteogenesis of bone marrow-derived mesenchymal stem cells by a functionalized silk fibroin hydrogel for bone defect repair. *Adv. Healthc. Mater.* **2019**, *8*, e1801043. [[CrossRef](#)] [[PubMed](#)]
35. Chien, K.B.; Makridakis, E.; Shah, R.N. Three-dimensional printing of soy protein scaffolds for tissue regeneration. *Tissue Eng. Part C Methods* **2013**, *19*, 417–426. [[CrossRef](#)]
36. Chien, K.B.; Shah, R.N. Novel soy protein scaffolds for tissue regeneration: Material characterization and interaction with human mesenchymal stem cells. *Acta Biomater.* **2012**, *8*, 694–703. [[CrossRef](#)]
37. Chen, B.-Q.; Kankala, R.K.; Chen, A.-Z.; Yang, D.-Z.; Cheng, X.-X.; Jiang, N.-N.; Zhu, K.; Wang, S.-B. Investigation of silk fibroin nanoparticle-decorated poly (l-lactic acid) composite scaffolds for osteoblast growth and differentiation. *Int. J. Nanomed.* **2017**, *12*, 1877–1890. [[CrossRef](#)]
38. Karageorgiou, V.; Kaplan, D. Porosity of 3D biomaterial scaffolds and osteogenesis. *Biomaterials* **2005**, *26*, 5474–5491. [[CrossRef](#)]
39. Castilho, M.; Moseke, C.; Ewald, A.; Gbureck, U.; Groll, J.; Pires, I.; Tessmar, J.; Vorndran, E. Direct 3D powder printing of biphasic calcium phosphate scaffolds for substitution of complex bone defects. *Biofabrication* **2014**, *6*, 15006. [[CrossRef](#)]
40. Li, J.; Zhi, W.; Xu, T.; Shi, F.; Duan, K.; Wang, J.; Mu, Y.; Weng, J. Ectopic osteogenesis and angiogenesis regulated by porous architecture of hydroxyapatite scaffolds with similar interconnecting structure in vivo. *Regen. Biomater.* **2016**, *3*, 285–297. [[CrossRef](#)]

41. Mygind, T.; Stiehler, M.; Baatrup, A.; Li, H.; Zou, X.; Flyvbjerg, A.; Kassem, M.; Bunger, C. Mesenchymal stem cell ingrowth and differentiation on coralline hydroxyapatite scaffolds. *Biomaterials* **2007**, *28*, 1036–1047. [[CrossRef](#)] [[PubMed](#)]
42. Deligianni, D.D.; Katsala, N.D.; Koutsoukos, P.G.; Missirlis, Y.F. Effect of surface roughness of hydroxyapatite on human bone marrow cell adhesion, proliferation, differentiation and detachment strength. *Biomaterials* **2001**, *22*, 87–96. [[CrossRef](#)]
43. Ionita, M.; Pandele, M.A.; Iovu, H. Sodium alginate/graphene oxide composite films with enhanced thermal and mechanical properties. *Carbohydr. Polym.* **2013**, *94*, 339–344. [[CrossRef](#)] [[PubMed](#)]
44. Bayraktar, H.H.; Morgan, E.F.; Niebur, G.L.; Morris, G.E.; Wong, E.K.; Keaveny, T.M. Comparison of the elastic and yield properties of human femoral trabecular and cortical bone tissue. *J. Biomech.* **2004**, *37*, 27–35. [[CrossRef](#)]
45. Wang, X.; Ma, J.; Wang, Y.; He, B. Structural characterization of phosphorylated chitosan and their applications as effective additives of calcium phosphate cements. *Biomaterials* **2001**, *22*, 2247–2255. [[CrossRef](#)]
46. Wang, X.; Ma, J.; Wang, Y.; He, B. Bone repair in radii and tibias of rabbits with phosphorylated chitosan reinforced calcium phosphate cements. *Biomaterials* **2002**, *23*, 4167–4176. [[CrossRef](#)]
47. Wang, X.; Ma, J.; Feng, Q.; Cui, F. Skeletal repair in of rabbits with calcium phosphate cements incorporated phosphorylated chitin reinforced. *Biomaterials* **2002**, *23*, 4591–4600. [[CrossRef](#)]
48. Wang, X.; Ma, J.; Feng, Q.; Cui, F. In vivo testing of S-chitosan enhanced calcium phosphate cements. *J. Bioact. Compat. Polym.* **2003**, *18*, 259–271. [[CrossRef](#)]
49. Wang, X.; Ma, J.; Feng, Q.; Cui, F. The effects of S-chitosan on the physical properties of calcium phosphate cements. *J. Bioact. Compat. Polym.* **2003**, *18*, 45–57. [[CrossRef](#)]
50. Kokubo, T.; Takadama, H. How useful is SBF in predicting in vivo bone bioactivity? *Biomaterials* **2006**, *27*, 2907–2915. [[CrossRef](#)]
51. Zhu, P.; Masuda, Y.; Koumoto, K. The effect of surface charge on hydroxyapatite nucleation. *Biomaterials* **2004**, *25*, 3915–3921. [[CrossRef](#)] [[PubMed](#)]
52. Turk, S.; Altinsoy, I.; Celebi Efe, G.; Ipek, M.; Ozacar, M.; Bindal, C. 3D porous collagen/functionalized multiwalled carbon nanotube/chitosan/hydroxyapatite composite scaffolds for bone tissue engineering. *Mater. Sci. Eng. C Mater. Biol. Appl.* **2018**, *92*, 757–768. [[CrossRef](#)] [[PubMed](#)]
53. Wang, X. Overview on biocompatibilities of implantable biomaterials. In *Advances in Biomaterials Science and Biomedical Applications in Biomedicine*; Lazinic, R., Ed.; In Tech: Rijeka, Croatia, 2013; pp. 111–155.
54. Zhao, X.; Liu, L.; Wang, J.; Xu, Y.F.; Zhang, W.M.; Khang, G.; Wang, X. In vitro vascularization of a combined system based on a 3D bioprinting technique. *J. Tissue Eng. Regen. Med.* **2014**, *10*, 833–842. [[CrossRef](#)] [[PubMed](#)]
55. Lei, M.; Wang, X. Biodegradable polymers and stem cells for bioprinting. *Molecules* **2016**, *21*, 539. [[CrossRef](#)] [[PubMed](#)]
56. Wang, X. Spatial effects of stem cell engagement in 3D printing constructs. *J. Stem Cells Res. Rev. Rep.* **2014**, *1*, 5–9.
57. Wang, X.; Xu, H. Incorporation of DMSO and dextran-40 into a gelatin/alginate hydrogel for controlled assembled cell cryopreservation. *Cryobiology* **2010**, *61*, 345–351. [[CrossRef](#)]
58. Saravanan, S.; Chawla, A.; Vairamani, M.; Sastry, T.P.; Subramanian, K.S.; Selvamurugan, N. Scaffolds containing chitosan, gelatin and graphene oxide for bone tissue regeneration in vitro and in vivo. *Int. J. Biol. Macromol.* **2017**, *104*, 1975–1985. [[CrossRef](#)]
59. Meskinfam, M.; Bertoldi, S.; Albanese, N.; Cerri, A.; Tanzi, M.C.; Imani, R.; Baheiraei, N.; Farokhi, M.; Fare, S. Polyurethane foam/nano hydroxyapatite composite as a suitable scaffold for bone tissue regeneration. *Mater. Sci. Eng. C Mater. Biol. Appl.* **2018**, *82*, 130–140. [[CrossRef](#)]
60. Wang, X.; Ao, Q.; Tian, X.; Fan, J.; Wei, Y.; Hou, W.; Tong, H.; Bai, S. 3D bioprinting technologies for hard tissue and organ engineering. *Materials* **2016**, *9*, 802. [[CrossRef](#)]
61. Wang, X.; Ao, Q.; Tian, X.; Fan, J.; Wei, Y.; Tong, H.; Hou, W.; Bai, S. Gelatin-based hydrogels for organ 3D bioprinting. *Polymers* **2017**, *9*, 401. [[CrossRef](#)]
62. Li, S.; Tian, X.; Fan, J.; Tong, H.; Ao, Q.; Wang, X. Chitosans for tissue repair and organ three-dimensional (3D) bioprinting. *Micromachines* **2019**, *10*, 765. [[CrossRef](#)] [[PubMed](#)]
63. Wang, X.; Liu, C. Fibrin hydrogels for endothelialized liver tissue engineering with a predesigned vascular network. *Polymers* **2018**, *10*, 1048. [[CrossRef](#)] [[PubMed](#)]

64. Liu, L.; Wang, X. Hared tissue and organ manufacturing. In *Organ Manufacturing*; Wang, X., Ed.; Nova Science Publishers Inc.: New York, NY, USA, 2015; pp. 301–333.
65. Liu, L.; Zhou, X.; Xu, Y.; Zhang, W.M.; Liu, C.-H.; Wang, X.H. Controlled release of growth factors for regenerative medicine. *Curr. Pharm. Des.* **2015**, *21*, 1627–1632. [[CrossRef](#)] [[PubMed](#)]
66. Xu, Y.; Wang, X. 3D biomimetic models for drug delivery and regenerative medicine. *Curr. Pharm. Des.* **2015**, *21*, 1618–1626. [[CrossRef](#)] [[PubMed](#)]
67. Wang, X. Advanced polymers for three-dimensional (3D) organ bioprinting. *Micromachines* **2019**, *10*, 814. [[CrossRef](#)] [[PubMed](#)]
68. Wang, X.; Liu, C. 3D bioprinting of adipose-derived stem cells for organ manufacturing. In *Enabling Cutting Edge Technology for Regenerative Medicine*; Springer: Singapore, 2018; Chapter 1; pp. 3–14.
69. Wang, X. Bioartificial organ manufacturing technologies. *Cell Transplant.* **2018**, *27*, 1–13. [[CrossRef](#)] [[PubMed](#)]
70. Tatavarty, R.; Ding, H.; Lu, G.; Taylor, R.J.; Bi, X. Synergistic acceleration in the osteogenesis of human mesenchymal stem cells by graphene oxide-calcium phosphate nanocomposites. *Chem. Commun.* **2014**, *50*, 8484–8487. [[CrossRef](#)]
71. Bressan, E.; Ferroni, L.; Gardin, C.; Sbricoli, L.; Gobbato, L.; Ludovichetti, F.S.; Tocco, I.; Carraro, A.; Piattelli, A.; Zavan, B. Graphene based scaffolds effects on stem cells commitment. *J. Transl. Med.* **2014**, *12*, 296. [[CrossRef](#)]
72. Wei, G.; Gong, C.; Hu, K.; Wang, Y.; Zhang, Y. Biomimetic hydroxyapatite on graphene supports for biomedical applications: A review. *Nanomaterials* **2019**, *9*, 1435. [[CrossRef](#)]
73. LeGeros, R.Z. Calcium phosphate-based osteoinductive materials. *Chem. Rev.* **2008**, *108*, 4742–4753. [[CrossRef](#)]



© 2020 by the authors. Licensee MDPI, Basel, Switzerland. This article is an open access article distributed under the terms and conditions of the Creative Commons Attribution (CC BY) license (<http://creativecommons.org/licenses/by/4.0/>).